Composites Part B 247 (2022) 110312

Contents lists available at ScienceDirect

Composites Part B

journal homepage: www.elsevier.com/locate/compositesb

Silicone rubber matrix composites with shear thickening fluid microcapsules realizing intelligent adaptation to impact loadings

J.Q. Zhu [a,b,e,1], Z.P. Gu [a,c,1], Z.P. Liu [b,**], F.C. Zhong [b], X.Q. Wu [a,c,*], C.G. Huang [c,d]

[a] Key Laboratory of Mechanics in Fluid Solid Coupling Systems, Institute of Mechanics, Chinese Academy of Sciences, Beijing, 100190, China
[b] Institute of Chemical Materials, China Academy of Engineering Physics, Mianyang, 621900, China
[c] School of Engineering Science, University of Chinese Academy of Sciences, Beijing, 100049, China
[d] Hefei Institutes of Physical Science, Chinese Academy of Sciences, Heifei, 230031, China
[e] CAS Key Laboratory for Biomedical Effects of Nanomaterials and Nanosafety, National Center for Nanoscience and Technology (NCNST), Beijing, 100190, PR China

ARTICLE INFO

Keywords:
SR-STF composites
Intelligent adaptation
Strain-rate sensitivity
Hyper-viscoelastic constitutive model

ABSTRACT

In this paper, silicone rubber matrix composites with shear thickening fluid microcapsules (SR-STF) with intelligent adaptation to impact loadings are fabricated for advanced impact protective structure. The composites exhibit more flexibility at low strain rates but higher stiffness at high loading rates, indicating significant strain-rate sensitivity. In addition, the initial flexibility and the strain-rate sensitivity of the composite increase with increasing the mass fraction of the STF microcapsules, which should be ascribed to the shear thickening and compressive jamming of the STF microcapsules in the composite during impulse loadings. Based on experimental results, a hyper-viscoelastic constitutive model is developed, in which the influence of the mass fraction of STF microcapsules, the strain-rate sensitivity, and the strain-hardening effect are taken into account. The paper develops a practical strategy for applications of STF in soft protective structures and provides a reliable prediction of the dynamic mechanical behavior of the SR-STF composites.

1. Introduction

Impact resistance and vibration attenuation of materials have attracted great attention in a variety of engineering applications [1–3]. In recent years, advanced protective materials with reversible energy absorption and adequate flexibility are required urgently in some specific applications such as soft body armor [4–6]. The traditional protective materials such as high-performance fiber-reinforced composites and ceramics generally show less flexibility [7,8], and their impact resistances are partially or completely lost after a single severe impact, restricting their applications in engineering structures subjected to multiple impacts [9–11].

Shear thickening (ST) materials, a kind of smart materials, have drawn great attention due to their reversibly sensitive response to external impact loadings [12,13]. At present, ST materials are generally divided into shear thickening gel (STG) and shear thickening fluid (STF) [14,15]. Both the STG and the STF have shown great prospects as impact-resistance materials [16,17]. STG is a gel-like boron-siloxane polymer blend with a low crosslinking degree, while STF is a type of non-Newtonian suspension liquid composed of high content of dispersed phase particles and liquid dispersion media. Generally, STF have a relatively low initial viscosity and exhibits a fluid to solid transition under the actions of an external transient force [18]. Therefore, STF is generally more flexible at initial state [19,20]. In addition, it is also suitable for anti-high-impact loading considering that the dispersed phase particles of STF is generally rigid inorganic nanoparticles [21].

Various mechanisms have been developed to explain the thickening behavior of STF. The order-to-disorder transformation is firstly developed by Hoffman [22]. It seems, however, experimentally unnecessary. The hydro-cluster of particles in STF is generally regarded as the reason for shear thickening under shear loadings [23–25] and the dynamic solidification is observed under compression at high loading rates [21,26]. During the thickening of STF, remarkable energy is dissipated [27–31]. More importantly, the STF recoveries quickly to its initial state

* Corresponding author. Key Laboratory of Mechanics in Fluid Solid Coupling Systems, Institute of Mechanics, Chinese Academy of Sciences, Beijing, 100190, China.
** Corresponding author. Institute of Chemical Materials, China Academy of Engineering Physics, Mianyang, 621900, China.
E-mail addresses: liuzp@caep.cn (Z.P. Liu), wuxianqian@imech.ac.cn (X.Q. Wu).
[1] These authors contributed equally to this work.

https://doi.org/10.1016/j.compositesb.2022.110312
Received 21 May 2022; Received in revised form 8 September 2022; Accepted 22 September 2022
Available online 28 September 2022

after removing loadings, showing a reversible energy absorption behavior [28,32,33]. Due to the unique properties of STF, it has been widely used in shock absorbers, dampers, control devices, etc. [34–36].

Since STF is fluid by nature and sensitive to environment, it needs to be properly encapsulated in practical application. Gürgen et al. [36,37] impregnated fabric composites with STF to enhance the stab and impact resistance while keeping flexibility. The study by Gürgen et al. [38,39] also showed that the join of STF in cork composite structures improved the impact performance. Sofuoğlu et al. [40] used the carbon fiber reinforced polymer tubes filled with STF to increase the vibration attenuation. Wu et al. [41,42] sealed the STF by metallic lattice sandwich panels, and the energy absorption behavior of STF-filled lattice sandwich panels showed the "1 + 1»2" effect, i.e. the strength of the sandwich panel with the STF filled pyramidal lattice truss core was also much higher than the adding result of pure STF and the sandwich panel with empty truss core.

However, the aforementioned metallic skeletons for sealing STF are almost rigid, and the leakage of the STF cemented on fibers will occur after relative long-term storage. Therefore, it is required to develop a perfect sealing material with flexibility and invulnerability to environment to broaden the usage of STF. Silicone rubber has been widely used as a sealant and energy absorption material in engineering. Sealing the STF microcapsules with silicone rubber, it is expected to realize not only sufficient flexibility, but also excellent energy absorption capacity, which could be used in advanced soft protective structures such as bulletproof helmet lining to provide adequate flexibility at low loading rates but contribute efficiently energy absorption under high-velocity impact.

In this paper, the silicone rubber composites with STF microcapsules (SR-STF) are fabricated and their mechanical behavior is investigated for the first time. Under quasi-static and dynamic loading testing, the composites show intelligent adaptation to the loading rates. It is more flexible under quasi-static loadings but has higher stiffness at high loading rates, providing a practical strategy for applications of STF in soft protective structures. In addition, the initial flexibility and the strain-rate sensitivity increase significantly with increasing the mass fraction of the STF capsules. Based on experimental results, a hyper-viscoelastic constitutive model is developed for the SR-STF composites, in which the effects of the mass fraction of STF microcapsules, the strain-rate sensitivity, and the strain hardening are considered, providing an accurate prediction of the mechanical behavior of the SR-STF composites.

The paper is organized as follows. In Section 2, the method for preparing the SR-STF material is described, and the modified split Hopkinson bar testing of the SR-STF composites is introduced. In Section 3, the experimental measurement results of the SR-STF composites are provided, and the effects of mass fraction of STF microcapsules and the strain-rate sensitivity are discussed. In Section 4, a hyper-viscoelastic constitutive model for the SR-STF composites is developed based on the experimental results, followed by discussion and conclusions.

2. Materials fabrication and experimental methods

2.1. Fabrication of STF

The colloidal nanoparticles were prepared by means of the improved Stöber method [43,44]. First, a certain amount of ammonia and anhydrous ethanol were mixed evenly in a reactor. Then, with mechanical agitation under the temperature of 40 °C, the evenly mixed ethanol dispersion of tetraethyl orthosilicate was added to the reactor by a peristaltic pump at a certain speed. After the dripping was completed, the temperature was kept at 40 °C and the mixture was stirred mechanically for 2 h. Finally, most of the solvent is removed by evaporation to produce silica nanoparticle concentrated disperse liquid, in which the mass fraction of silica nanoparticle is 12.5%. The silica nanoparticle concentrated disperse liquid is then mixed with PEG-200 by mechanical

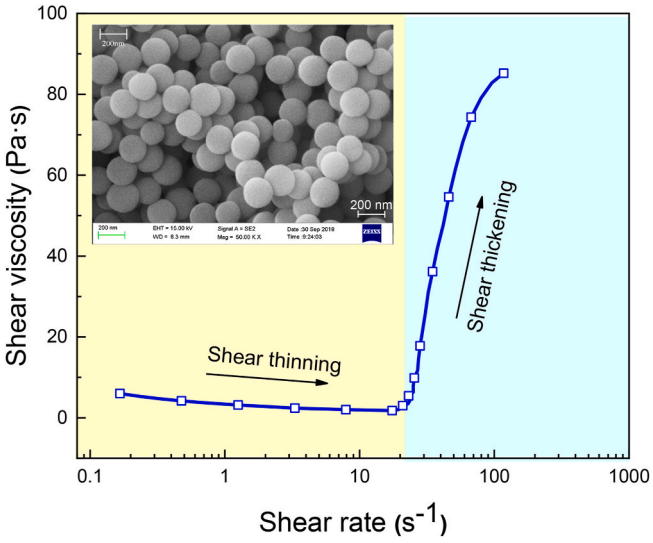

Fig. 1. Steady-state shear viscosities of the STF at various strain rates, showing an initial shear thinning behavior, followed by a discontinuous shear thickening behavior.

stirring. After that, the dispersion was rotated-steamed and the ethanol was removed to obtain the STF. In the present study, the particle mass fraction of the STF is 67.5%. The SiO_2 nanoparticles were characterized by UItra 55 (Zeiss, Germany) field-emission scanning electron microscope. The rheological property of STF was tested by Kinexus Pro rotary rheometer (Malvern, UK). The diameter of lamina was 40 mm with a cone angle of 1°. The spacing was 0.03 mm, and the temperature was 25 °C. As shown in Fig. 1, the SiO_2 nanoparticles are nearly mono-disperse with an average diameter of 200 nm with less than 10% poly-dispersity. When the shear strain rate exceeds the critical value of 21 s^{-1}, the shear thickening behavior occurs as evidenced by the abrupt increase of viscosity.

2.2. Fabrication of SR-STF composites

The SR-STF composites were fabricated through emulsifying and curing processes. The STF with a certain weight, the Sylard® 184 silicone elastomer purchased from Dow Corning, and the curing agent component were mixed in a container. Since the STF would affect the vulcanization of the silicone rubber, an additional Pt catalyst (Pt content 3000 ppm) was also used to promote the vulcanization of the silicone rubber. After emulsifying with a mechanical agitator at 300 r/min for 6 min, the mixture was defoamed in a vacuum defoaming machine and then poured into a mold for curing at 80 °C in an air blast drying oven. After demolding, the silicone rubber composites with STF microcapsules were fabricated for tests. The schematic diagram for preparing the SR-STF composites is depicted in Fig. 2.

Five kinds of SR-STF composites, i.e. SR-STF-0 without STF, SR-STF-10 with 10 wt% STF, SR-STF-20 with 20 wt% STF, SR-STF-30 with 30 wt % STF, and SR-STF-40 with 40 wt% STF were fabricated. The structures of the SR-STF composites were characterized by Axio Lab. A1 (Zeiss, Germany) optical microscope (OM) with a CCD Camera and UItra 55 (Zeiss, Germany) field-emission scanning electron microscope (FESEM). It can be seen from the optical microscopy photos in Fig. 3, the STF was dispersed almost evenly in the silicone rubber matrix in the form of spherical microcapsules for all the SR-STF composites. Most of the STF microcapsules are isolated from each other. The diameters of the STF microcapsules in all the SR-STF composites have relative wide distributions from 5 to 25 μm. The average diameters of the STF microcapsules for the SR-STF-10, the SR-STF-20, the SR-STF-30, and the SR-STF-40 are 13.7 ± 5.0, 13.2 ± 4.2, 13.4 ± 4.5, and 10.2 ± 2.1 μm, respectively. For the SR-STF-40, the average diameter of the STF microcapsules

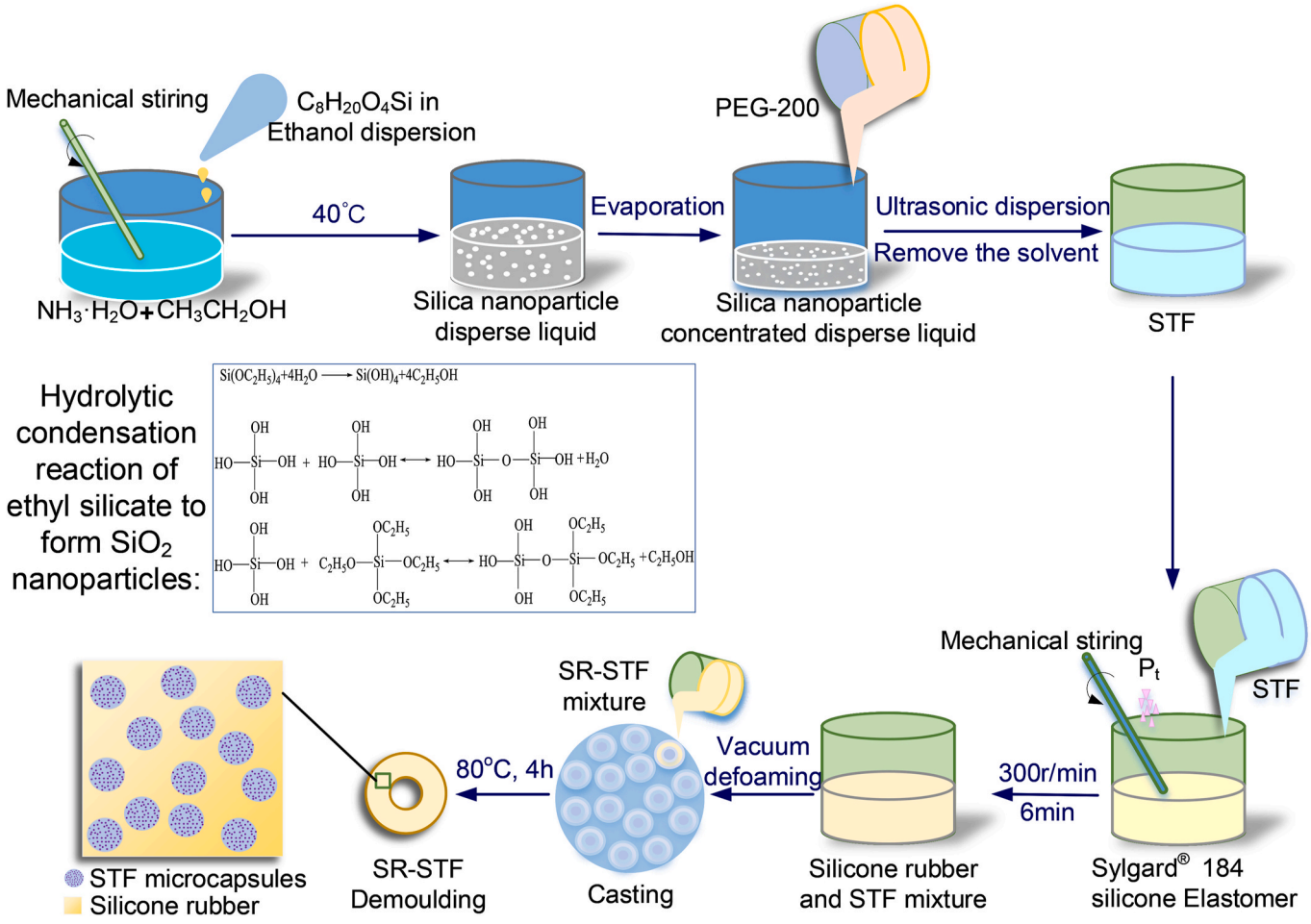

Fig. 2. Schematic diagram for preparing the SR-STF composites.

is a little smaller than the other composites. More precisely control procedure will be investigated in future.

2.3. Compressive testing methods

The quasi-static compressive mechanical behavior of the SR-STF composites was measured by a universal testing machine. The sizes of the specimens were Φ29 × 12.5 mm. The compressive speeds varied from 0.75 to 75 mm/min, corresponding to strain rates 10^{-3} to 10^{-1} s^{-1}. The dynamic compressive mechanical behavior of the SR-STF composites was measured by a modified split Hopkinson pressure bar (SHPB) [45,46]. As shown in Fig. 4, the facility comprises a striker bar, an incident bar, and a transmitted bar that are made of 7075-T6 aluminum alloy with a nominal yield strength of approximately 500 MPa. The sizes of the strike bar, the incident bar, and the transmitted bar are Φ19.05 × 400 mm, Φ19.05 × 1800 mm, and Φ19.05 × 1500 mm, respectively. Since the SR-STF composites have very low impedance, it is hard to measure exactly the transmitted stress. Therefore, a hollow transmitted bar with an outer diameter of 19.05 mm and an inner diameter of 12.05 mm was used to amplify the transmitted signals. The striker bar was accelerated using a gas gun. The rubber pulse shapers with a diameter of 1 mm and a thickness of 0.25 mm were used in experiments to ensure the stress equilibrium in the specimen during loading and to achieve constant loading rate conditions.

When the strike bar impacts the incident bar, the incident compressive wave, denoted by $\varepsilon_I(t)$, is generated and propagates towards the specimen. Due to the impedance mismatch between the specimen and the incident bar, part of the incident compressive wave reflects into the incident bar, denoted by $\varepsilon_R(t)$, while the rest denoted by $\varepsilon_T(t)$ transmits into the tube-shaped transmitted bar. Based on the one-dimensional elastic stress wave theory and the assumption of homogeneous deformation, the engineering stress $\sigma_S(t)$, the strain rates $\dot{\varepsilon}_S(t)$, and strain $\varepsilon_S(t)$ in the specimen can be calculated as follows,

$$\sigma = E\frac{A_0}{A_S}\varepsilon_T(t) \tag{1}$$

$$\varepsilon = -\frac{2c_0}{l_S}\int_0^t \varepsilon_R(\tau)d\tau \tag{2}$$

$$\dot{\varepsilon} = -\frac{2c_0}{l_s}\varepsilon_R(t) \tag{3}$$

where A_S and A_0 are cross-section areas of the specimen and the bar, respectively, c_0 is elastic longitudinal stress wave speed, and l_s is thickness of the specimen.

2.4. Shape design of specimens

It is known that the SHPB testing will introduce errors due to the inertia effect, which is not negligible for soft materials like the SR-STF composites [47–50]. Annular-shaped specimens with an outer radius a and an inner radius b are designed to decrease effectively the extra stress [49]. The radial inertial induced extra axial stress for incompressible

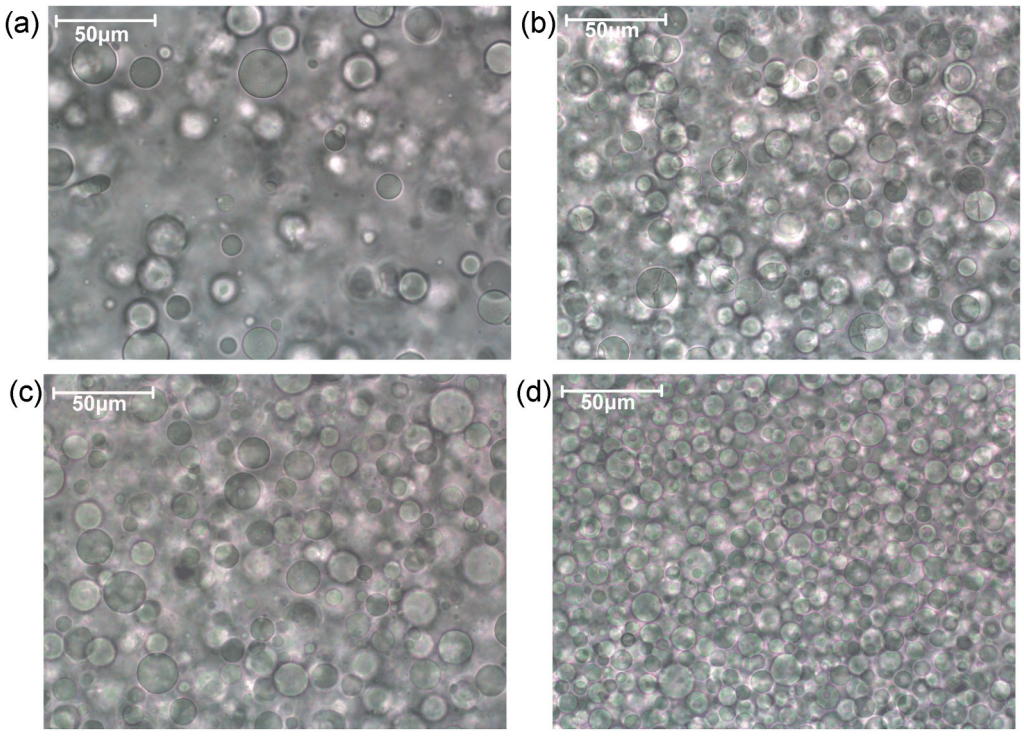

Fig. 3. Microstructures of (a) SR-STF-10, (b) SR-STF-20, (c) SR-STF-30, and (d) SR-STF-40, showing the almost even dispersion of the spherical STF microcapsules in the silicone rubber matrix.

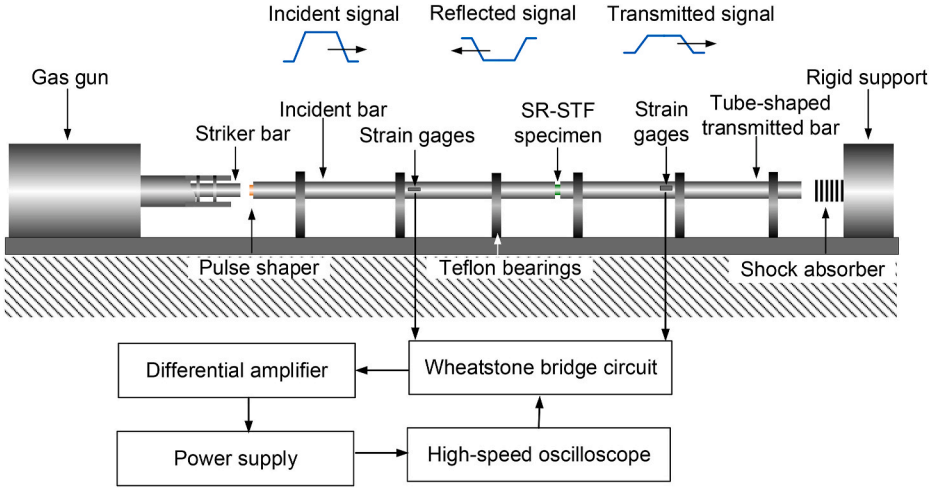

Fig. 4. Schematic diagram of SHPB testing.

materials is given as

$$\sigma_z^1 = \left\{ \rho_s \left(\frac{a^2 + b^2 - r^2}{4} \right) - \frac{3\rho_s a^2 b^2}{8E_S} \left[\rho_s \, ln\left(\frac{a}{r}\right)\omega^2 + \frac{3E_S}{3a^2} \right] \cos \omega t \right\} \ddot{\varepsilon} \tag{4}$$

where E_s and ρ_0 are Young's modulus and density, respectively. ω is constant as

$$\omega = \sqrt{\frac{2E_s\left(b^2 - a^2\right)}{3\rho_s \ln\left(\frac{b}{a}\right) b^2 a^2}} \tag{5}$$

The average inertia stress over the cross-section is

$$\overline{\sigma}_z^1 = \rho_S \left[\frac{a^2 + b^2}{8} - \frac{\left(b^2 - a^2\right)}{8 \ln\left(\frac{b}{a}\right)} \cos \theta t \right] \ddot{\varepsilon}_z \tag{6}$$

Fig. 5 shows the radial distributions of the extra axial stress of a solid specimen with a radius of 6.5 mm and an annular-shaped specimen with an outer radius of 6.5 mm and an inner radius of 2.5 mm, where Young's modulus of the specimen E_s is 4.0 MPa, the density ρ_s is 1150 kg/m^3, and the strain rate differential $\ddot{\varepsilon}$ is 1.0×10^8 s^{-2}. It can be seen that for the solid specimen, extra axial stress decreases along the radial direction, and the maximum extra axial stress is 1.21 MPa. However, for the annular specimen, the maximum extra axial stress is 0.24 MPa, a significant reduction of 80% when compared to that of the solid specimen.

For the SHPB experiments with relative high loading rates, the fric-

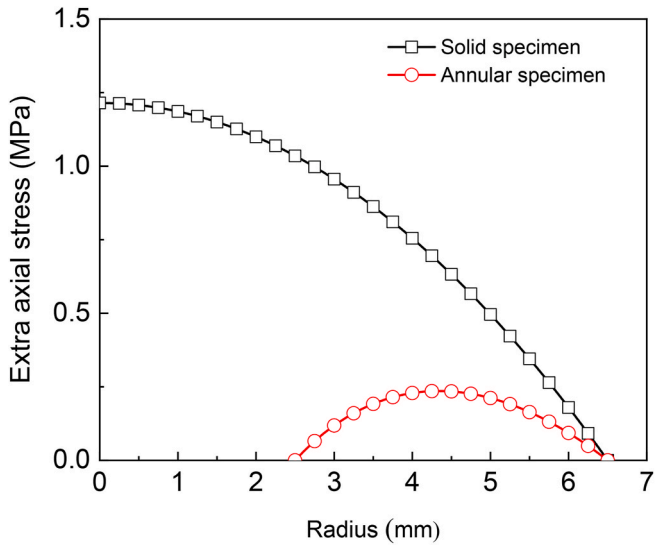

Fig. 5. Stress distributions induced by radial inertia in a solid specimen and an annular-shaped specimen.

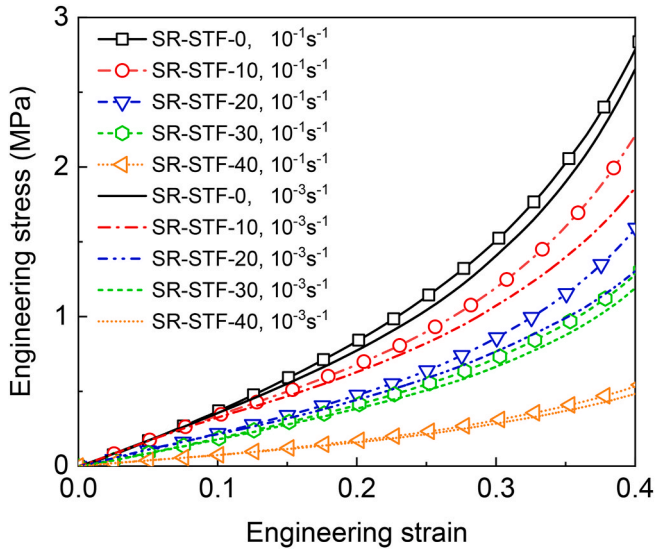

Fig. 6. Engineering stress versus engineering strain curves under strain rates of 10^{-3} s^{-1} and 10^{-1} s^{-1}.

tion between the specimen and the bars will influence the experimental results [51,52]. For soft materials with low stiffness, friction between bars and specimens has a great impact on the measurement results. Klepaczko and Malinowski [53,54] developed a method to diminish the friction effect,

$$\sigma = \sigma_0\left(1 - \frac{2\theta r}{3h}\right) \tag{7}$$

where σ is corrected stress, σ_0 is measured stress, θ is friction coefficient, r and h are radius and thickness of specimen, respectively. Eq. (7) indicates that the smaller the thickness to radius ratio, the higher friction-induced extra stress. In addition, the silicone lubricant is used to decrease significantly the friction between the specimen and the bars. By considering the effects of friction and stress equilibrium during dynamic compression [47], the thickness of the specimens is determined as 2.5 mm. Therefore, the annular specimens with outer radius 6 mm, inner radius 2.5 mm, and thickness 2.5 mm are prepared for the SHPB tests.

3. Experimental results

The mechanical behaviors of the SR-STF composites with various mass fractions of STF microcapsules, i.e. SR-STF-0, SR-STF-10, SR-STF-20, SR-STF-30, SR-STF-40, are measured under different loading rates.

3.1. Mechanical behavior of the SR-STF composites under low strain rates

The engineering stress-strain relationships of the SR-STF composites under strain rates ranging from 10^{-3} to 10^{-1} $s^{-1}$are shown in Fig. 6. The results indicate that all of the five kinds of composites show nonlinear elasticity for strain smaller than 0.4. Under the strain rate 10^{-1} s^{-1}, the stresses of the SR-STF-0, the SR-STF-10, the SR-STF-20, the SR-STF-30, and the SR-STF-40 are about 2.8, 2.2, 1.5, 1.1, and 0.5 MPa at strain 0.4, indicating that the stiffness of the composite decreases with increasing the mass fraction of STF microcapsules under low strain rates. Here, the stiffness or the flexibility of the material is represented by the stress at stain 0.35. The higher the stress, the higher the stiffness and the lower the flexibility of the SR-STF composites. It could be well understood by the mechanical behavior of the STF that below the critical strain rates of the STF, it acts as liquid and exhibits slight shear thinning behavior, leading to the weakening effect with increasing its content. The even low stiffness of the composite indicates the more flexibility of the material with increasing the mass fraction of STF microcapsules, which is strongly required for the design of soft impact protective structures. In addition, at the same strain, the stiffness under the strain rate 10^{-1} s^{-1} is obviously higher than that under the strain rate 10^{-3} s^{-1}, indicating obvious positive strain-rate sensitivity of the SR-STF composites.

3.2. Mechanical behavior of the SR-STF composites under high strain rates

The engineering stress-strain relationships of the SR-STF composites under high strain rates ranging from 1400 to 3500 s^{-1} are shown in Fig. 7. During dynamic loadings, to avoid the specimen running out of the sections of the pressure bars, the relationship between specimen diameter, bar diameter and engineering strain is given as [55].

$$d_0 = d_{bar}\sqrt{1-\varepsilon_E} \tag{8}$$

where $d_{bar} = 19.05\ mm$ is diameter of the incident and the transmitted bars, $d_0 = 13\ mm$ is diameter of the SR-STF composite specimens. From Eq. (8), the engineering strain ε_E should not exceed 0.53. As a result, the engineering stress-strain relationships for strain less than 0.4 are investigated in the present study. It can be seen that at the same strain, the stress increases with increasing strain rate, showing obvious positive strain-rate sensitivity for all the SR-STF composites. In addition, the stiffness decreases with the increase of the mass fraction of STF microcapsules. Under quasi-static loading condition, the stresses at strain 0.4 for the SR-STF-0 and the SR-STF-40 are 2.80 MPa and 0.47 MPa, respectively. However, under the strain rate of 3500 s^{-1}, the stresses at strain 0.4 for the SR-STF-0 and the SR-STF-40 are 8.45 MPa and 7.42 MPa, respectively, indicating that the difference in stiffness for the SR-STF composites varies in a narrower range under high strain rates when compared to that under low strain rates. At strain 0.4, with increasing the mass fraction of STF microcapsules from 0% to 40%, the stress decreases from 5.9 MPa to 4.2 MPa, a reduction of 29%, under strain rate 1400 s^{-1}, while it decreases from 8.0 MPa to 7.0 MPa, a reduction of 12.5%, under strain rate 3500 s^{-1}. The results imply that the composite with a high mass fraction of STF microcapsules is more sensitive to loading rates when compared to that with a low mass fraction of STF microcapsules. It can be speculated that after a critical strain rate, the stresses of the SR-STF composites might exceed the stress of the silicone rubber matrix. The strain-rate sensitivity of the SR-STF composites should be mainly contributed by the STF microcapsules. With

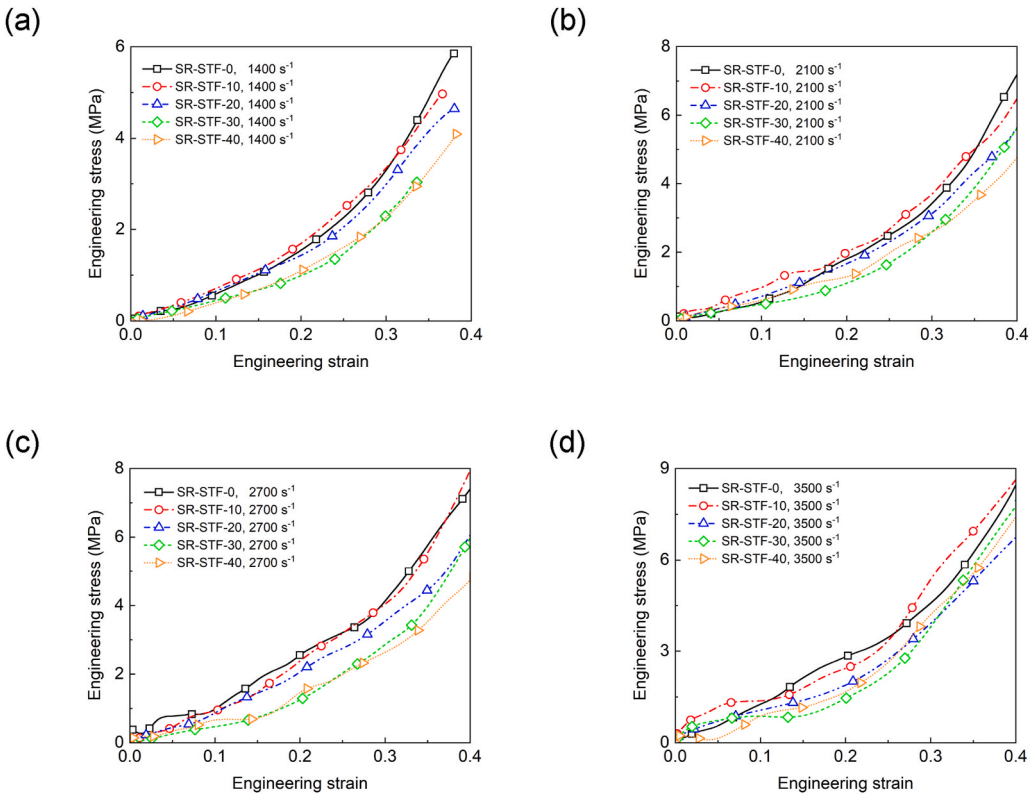

Fig. 7. Engineering stress versus engineering strain curves under high strain rates of (a) 1400s^{-1}, (b) 2100 s^{-1}, (c) 2700 s^{-1} and (d) 3500 s^{-1}.

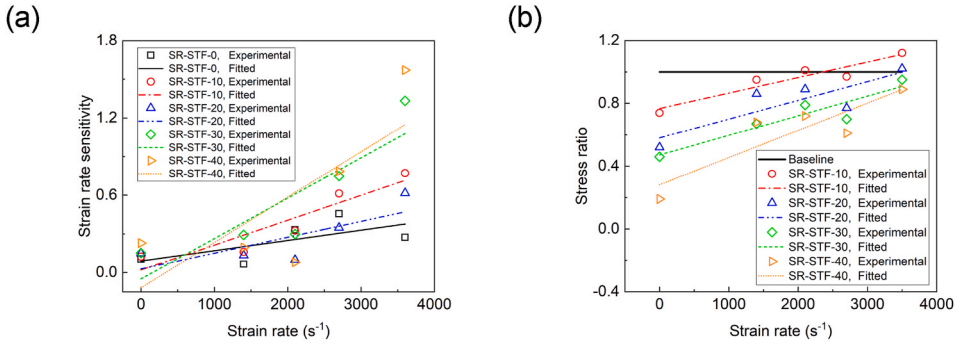

Fig. 8. (a) Strain-rate sensitivity exponent versus strain rate, showing more strain-rate sensitivity of composites with higher strain rates. (b) Stress ratio versus strain rate, showing that the stresses of the composites with high content of STF microcapsules trend to exceed that with low content of STF microcapsules.

increasing the loading rates, the squeeze speed of the STF microcapsules increases during compression, rendering higher compressive stresses of the STF microcapsules. As a result, with increasing the mass fraction of STF microcapsules, the SR-STF composite shows more sensitivity to loading rates.

Table 1
Parameters of fitting lines on strain rate sensitivity versus STF content.

Materials	SR-STF-0	SR-STF-10	SR-STF-20	SR-STF-30	SR-STF-40
Slope k_1	7.95 × 10^{-5}	1.93 × 10^{-4}	1.23 × 10^{-4}	3.13 × 10^{-4}	3.52 × 10^{-4}
Intercept b_1	9.05 × 10^{-2}	2.06 × 10^{-2}	2.79 × 10^{-2}	−4.92 × 10^{-2}	−1.18 × 10^{-1}

3.3. Summary of experimental results

To analyze the mechanical behavior of the SR-STF composites, the logarithmic strain rate sensitivity coefficient, m, and the stress ratio, φ, are employed. The logarithmic strain rate sensitivity coefficient, m, characterizes the strain rate effect,

$$m = \frac{dln\sigma_{\dot{\varepsilon}}}{dln\dot{\varepsilon}} \tag{9}$$

where $\dot{\varepsilon}$ is going to be 10^{-1} s^{-1}, 1400 s^{-1}, 2100 s^{-1}, 2700 s^{-1}, 3500 s^{-1}. σ is the engineering stress of the SR-STF-10, the SR-STF-20, the SR-STF-30, and the SR-STF-40 at the strain of 0.35. The stress ratio φ reflects the influence of STF content on the stiffness of the SR-STF composites,

$$\varphi = \frac{\sigma(\eta_2)}{\sigma(\eta_1)|_{\dot{\varepsilon}}} \tag{10}$$

Table 2
Parameters of fitting line on stress ratio versus STF content.

Materials	SR-STF-0	SR-STF-10	SR-STF-20	SR-STF-30	SR-STF-40
Slope k_2	0	8.5×10^{-5}	1.1×10^{-4}	1.3×10^{-4}	1.7×10^{-4}
Intercept b_2	1	0.8	0.6	0.4	0.2

where $\sigma\ (\eta_1)$ is the stress of pure silicone rubber at the strain of 0.35 and strain rate $\dot{\varepsilon}$, $\sigma\ (\eta_2)$ is the stress at the strain of 0.35 and strain rate $\dot{\varepsilon}$ in the SR-STF-10, the SR-STF-20, the SR-STF-30, or the SR-STF-40.

The relationships between the strain rate sensitivity exponent versus strain rate under with STF content increased from 0 to 40% are shown in Fig. 8(a). It can be seen that the strain rate sensitivity exponent of each material increases with increasing the strain rate, indicating more sensitivity of strain-rate strengthening effect at higher strain rates. In addition, the strain rate sensitivity exponent increases with increasing the STF content from 0 to 40%, indicating that the composite with higher STF content possesses more sensitivity of strain-rate strengthening effect. The increase tendencies of the strain-rate sensitivity exponents with increasing the strain rate are fitted by straight lines at different STF content to simplify the analysis, and the fitted slopes and intercepts are listed in Table 1 for different SR-STF composites.

Fig. 8(b) shows the relationships between the stress ratios and the applied strain rate of the SR-STF composites. The stress ratio reveals the upward trend with increasing the applied strain rate. Similarly, the tendencies are fitted by straight lines to simplify the analysis, and the fitted slopes and intercepts are listed in Table 2 for different materials. Taking $\varphi = 1$ of the SR-STF-0 as the baseline, it is clearly shown that the stress ratios of the other composites are smaller than the SR-STF-0 at 10^{-3} s^{-1}. The higher the STF content, the smaller the stress ratio. With increasing the applied strain rate, the stress ratios of the other composites increase quickly approaching the baseline. The higher the STF content, the faster the increase tendency, indicating more strain-rate sensitivity of the composite with higher STF content. The stress ratio of the SR-STF-10 exceeds that of the SR-STF-0 first at about 2300 s^{-1}, and the stress ratio of SR-STF-20 exceeds the baseline at about 3500 s^{-1}, implying the better performance of these two composites than the original silicone rubber matrix. It is reasonable to expect that the stress ratio of the SR-STF-30 and the SR-STF-40 will finally exceed that of the SR-STF-0 at high strain rates. In addition, according to the experimental results, the stress ratio of the SR-STF-40 should exceed all of the other composites at a sufficient high strain rate. However, due to the difficulty of stress equilibrium of such soft composites in achieving even high

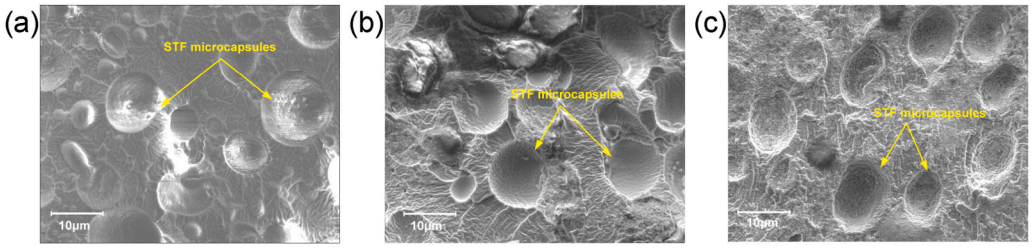

Fig. 9. Microstructures of the SR-STF-40 (a) before being impacted, (b) at the strain rate of 1400 s^{-1} s^{-1}, and (c) at the strain rate of 3500 s^{-1}. Severe deformation is observed under high loading rates.

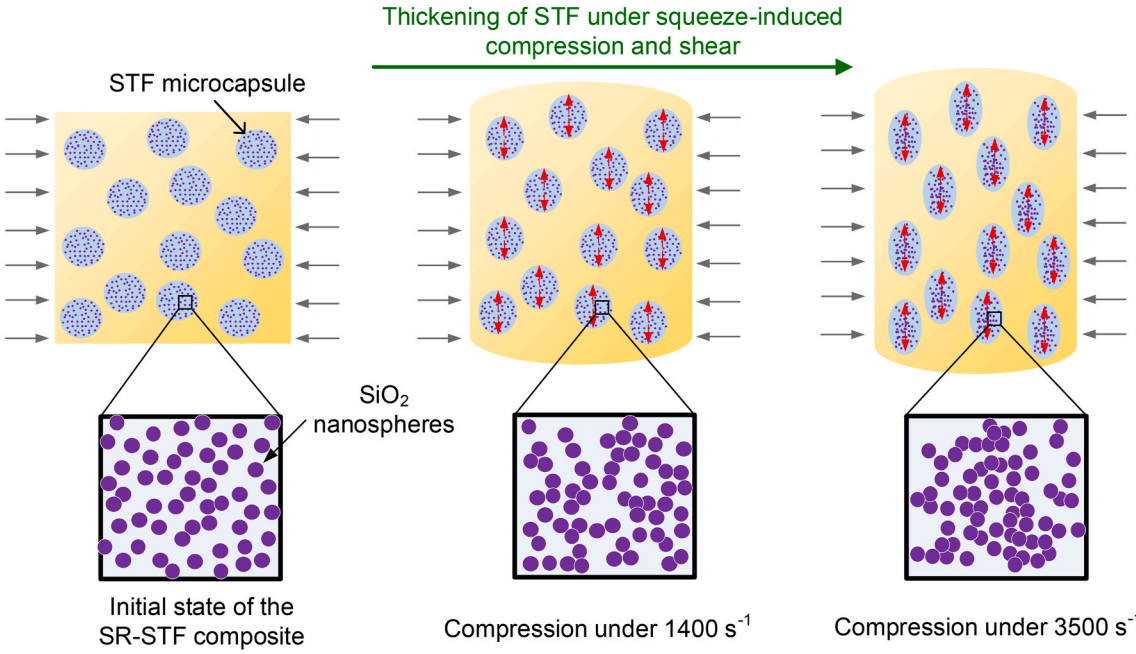

Fig. 10. Deformation behavior of the SR-STF composites under different strain rates. With increasing strain rate, the thickening behavior of the STF in the microcapsules occurs, providing high impact resistance.

strain rates during SHPB testing, this phenomenon is not directly observed in experiments.

3.4. Microstructures of the composites after compression

As the microstructure evolutions are similar for each composite, only the typical microstructures of the SR-STF-40 before compression, after compression at 1400 s^{-1}, and after compression at 3500 s^{-1} are shown in Fig. 9 (a), (b), and (c), respectively. It is clearly shown the compression behavior of the STF microcapsules as evidenced by the change of the shapes from near sphere to ellipsoid after experiments. The more severe deformations of the STF microcapsules are observed at a higher strain rate of 3500 s^{-1}. According to the microstructure evolution of the STF microcapsules, the experimental observation that the strain-rate strengthening sensitivity of the composite increases with increasing the contents of STF microcapsules and the loading rates can be well understood. As shown in Fig. 10, under quasi-static compression, the STF microcapsules are squeezed slowly under external stress. The STF inside the microcapsules are compressed along the loading direction, leading to the transverse shear flow. The initial viscosity of the STF provides negligible resistance during the compression due to the extremely low strain rate. In addition, the inertia of the STF microcapsules can also be neglected at low strain rates. As a result, the higher the STF content, the lower the stiffness of the composite at low strain rates as observed in experiments, making the composite with higher STF content more flexible. With increasing the strain rate of the compression, the shear rate will exceed the critical value of 21 s^{-1}, at which the thickening behavior of the STF occurs arising from particle clustering induced by hydrodynamic lubrication forces [22–24], rendering high resistance during transverse shear flow due to the significant increase of viscosity of the STF as shown in Fig. 1. In addition, the dynamic solidification of the STF microcapsules may occur under compression at high loading rates [26], which could also provide high resistance during compression of the composites. Therefore, the composite is more strain-rate sensitivity with increasing the loading rate and the STF content as shown in Fig. 8, providing excellent flexibility at low loading rates but high impact resistance at high loading rates for the composites with large STF content.

4. Constitutive model of the composites

4.1. Constitutive modeling

As the numerous STF microcapsules with diameters ranging from 5 to 25 μm are dispersed randomly in the specimens, the composites can be regarded as isotropic. According to the experimental results, the composites show hyper-elastic deformation behavior within a wide range of strain. In addition, it exhibits obvious strain-rate sensitivity. Moreover, the contents of STF microcapsules have a significant impact on the mechanical behavior of the composites. Therefore, the effects of hyper-elasticity, the strain-rate sensitivity, and the contents of STF microcapsules are considered in the constitutive model of the composites,

$$\sigma = \zeta(\varepsilon, \dot{\varepsilon})\xi(\eta) \tag{11}$$

where σ is the equivalent stress, ε and $\dot{\varepsilon}$ are strain and strain rate, η is mass fraction of STF microcapsules. As the Boltzmann superposition principle is widely employed to describe the strain hardening and strain rate effect of polymers [56–58], it is taken to described the mechanical behavior of the SR-STF composites,

$$\sigma = [\zeta_1(\varepsilon) + \zeta_2(\dot{\varepsilon})]\xi(\eta) \tag{12}$$

$\zeta_1(\varepsilon)$, $\zeta_2(\dot{\varepsilon})$ and $\xi(\eta)$ are the functions describing the effects of strain hardening, strain-rate strengthening, and content of STF microcapsules, respectively. Here, the influence of temperature is not considered, which will be investigated in future. The Ogden model, which is extensively used for rubbers, is used to describe the strain-hardening of the composite [59,60],

$$W = \sum_{i=1}^{3}\sum_{j=1}^{n}\frac{2\mu_j}{\alpha_j^2}(\overline{\lambda_i}^{\alpha_j} - 1) + k(J - 1 - lnJ) \tag{13}$$

where W is the strain energy density function, n is model order and taken 3 here, μ and α are model constants, k is bulk modulus, J is volume change coefficient. The relationship between $\overline{\lambda_i}$ and elongation ratio λ_i is

$$\overline{\lambda_i} = J^{-\frac{1}{3}}\lambda_i \tag{14}$$

In the present study, the composite is regarded as incompressible material and therefore J equals 1, $\overline{\lambda_i} = \lambda_i$. Consequently,

$$W = \sum_{i=1}^{3}\sum_{j=1}^{3}\frac{2\mu_j}{\alpha_j^2}\left(\lambda_i^{\alpha_j} - 1\right) \tag{15}$$

λ_1, λ_2, and λ_3 are elongation ratios along three orthogonal directions of elongation, respectively. Under uniaxial loading condition,

$$\lambda_1 = \lambda \tag{16}$$

$$\lambda_2 = \lambda_3 = \lambda^{-1/2} \tag{17}$$

$$\lambda = 1 + \varepsilon \tag{18}$$

where ε is engineering strain. As a result,

$$\sigma = \frac{dw}{d\lambda_1} = \sum_{j=1}^{3}\frac{2\mu_j}{\alpha_j}\left[\lambda_1^{\alpha_j - 1} - \lambda_1^{-\frac{\alpha_j}{2} - 1}\right] \tag{19}$$

where σ is uniaxial stress contributed by elastic deformation.

The Maxwell generalized model is employed to describe the strain-rate strengthening effect of the composites,

$$\sigma(t) = \int_0^t g(t-\tau)\frac{\partial\varepsilon}{\partial\tau}d\tau \tag{20}$$

where $g(t-\tau)$ is relaxation function,

$$g(t) = \sum_{i=1}^{n} G_i \exp(-\beta_i t) \tag{21}$$

therefore, under uniaxial loading condition, the stress contributed by strain-hardening and strain-rate strengthening is given as

$$\sigma = \sum_{j=1}^{3}\frac{2\mu_j}{\alpha_j}\left(\lambda_1^{\alpha_j - 1} - \lambda_1^{-\frac{\alpha_j}{2} - 1}\right) + \int_0^t \sum_{i=1}^{3} G_i \exp[-\beta_i(t-\tau)]\dot{\lambda}_1(\tau)d\tau \tag{22}$$

The effect of the content of STF microcapsules, η, is considered as follow,

$$\xi(\eta) = p\eta + 1 \tag{23}$$

where p is a parameter. According to the experimental results, the increase of the content of STF microcapsules leads to the decrease of the stiffness of the composite. Therefore, the parameter $p < 0$ at low strain rates, indicating a weakening effect of the content of STF microcapsule. However, the stiffness of the composite with a high content of STF mi-

Table 3
Constitutive parameters of hyper-elastic model.

μ_1/ MPa	μ_2/ MPa	μ_3/MPa	α_1	α_2	α_3
−95.83	51.63	45.28	−0.15	0.30	−0.55

Table 4
Constitutive parameters of viscoelastic model and p.

G_1	G_2	G_3	β_1	β_2	β_3	A	B
−3.35	38.25	−24.39	−92.65	−71.58	47.24	4.19×10^{-4}	−1.85

crocapsules trends to exceed that with a low content of STF microcapsules at high strain rates, showing a strengthening effect of the content of STF microcapsules. As a result, the parameter p should be a function of strain rate, which can be fitted by a linear function according to the experimental results as given in Fig. 8,

$$p = A\dot{\lambda}_1 + B \tag{24}$$

Therefore, the constitute model of the composites is given as follows, in which the strain hardening, strain-rate strengthening, influence of the content of STF microcapsules are considered,

$$\sigma = \left[\sum_{j=1}^{3}\frac{2\mu_j}{\alpha_j}\left(\lambda_1^{\alpha_j-1} - \lambda_1^{-\frac{\alpha_j}{2}-1}\right) + \int_0^t \sum_{i=1}^{3} G_i \exp[-\beta_i(t-\tau)]\dot{\lambda}_1(\tau)d\tau\right] \times [(A\dot{\lambda}_1 + B)\eta + 1] \tag{25}$$

The constitutive parameters as listed in Tables 3 and 4 are obtained based on the experimental results.

4.2. Validation and prediction of the constitutive model

To validate the constitutive model, the relationships between engineering stress and engineering strain of the SR-STF composites at the strain rates of 10^{-3} s^{-1} and 2700 s^{-1} are predicted as shown in Fig. 11. It could be seen that under the low strain rate of 10^{-3} s^{-1}, the constitutive model can predict the strain hardening effect for the pure SR and the SR-STF composites. When the engineering strain is larger than 0.35, the constitutive model slightly overestimates the stress of the SR-STF composites. Under the high loading rate of 2700 s^{-1}, the constitutive model can also predict the strain hardening effects of the pure SR and the SR-STF. However, for strain lower than 0.3, the constitutive slightly overestimates the stresses for the SR-STF-30 and the SR-STF-40. Overall, the effects of strain hardening, strain rate strengthen, and the mass fraction of STF microcapsules predicted by the constitutive model are reasonably agree with the experimental results, validating the constitutive model for describing the mechanical behavior of the SR-STF composites.

The measured and the calculated relationships between the engineering stresses at strain 0.35 and the strain rates are shown in Fig. 12, where the logarithm of strain rate is depicted to clearly show the strain-rate sensitivity. It can be seen that the calculation results are in agreement with the experimental results for different materials and strain rates. According to the experimental results and calculation results, the

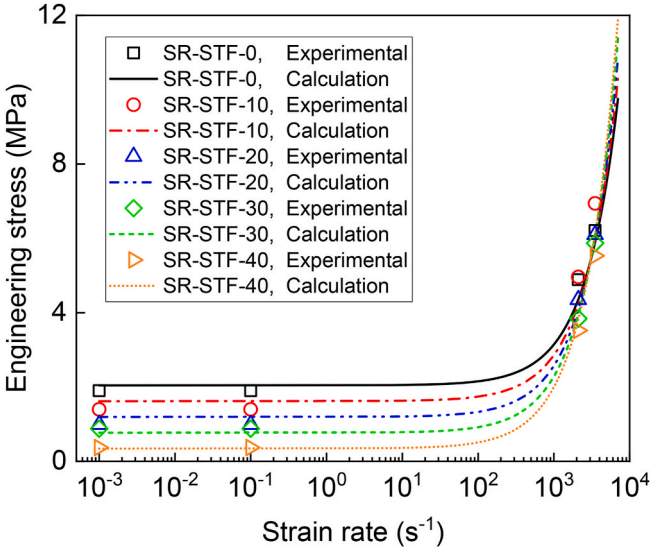

Fig. 12. Stress versus logarithm of strain rate of the SR-STF composites, showing a good agreement between the experimental results and the calculation results based on the constitutive model.

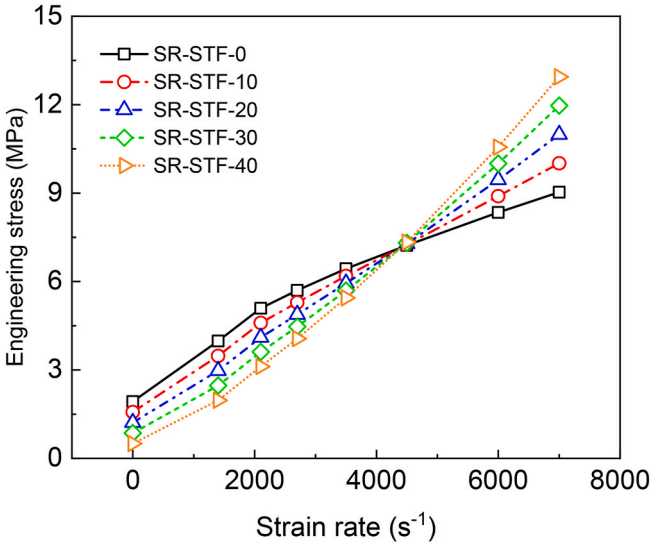

Fig. 13. Stress versus strain rate of the SR-STF composites. A critical strain rate is observed for all the composites. Below the critical strain rate, the stress increases with increasing strain rate and with decreasing the content of STF microcapsules. However, when the strain rate is higher than the critical strain rate, the stress increases with increasing strain rate and the content of STF microcapsules.

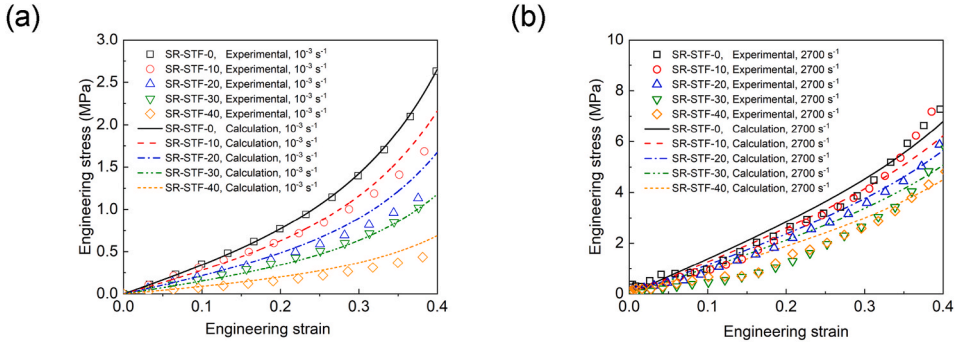

Fig. 11. Experimental results and the calculation results based on the constitutive model under the strain rates of (a) 10^{-3} s^{-1} and (b) 2700 s^{-1}.

stiffness of the composite increases slowly with increasing strain rate at the low strain-rate range, followed by the rapid increase process when the strain rate exceeds 10^3 s^{-1}. In addition, the stiffness of the composites with STF microcapsules trend to surpass that without STF microcapsules at the strain rate 10^3–10^4 s^{-1}. This phenomenon can be seen more clearly in Fig. 13. As the strain rates in experiments are not high enough due to the limitation of the experimental conditions, the calculated results at high strain rates are given based on the constitutive model as given by Eq. (25). It is clearly shown that the stresses of the composites increase with increasing strain rate, showing the positive strain-rate sensitivity. The engineering stresses of the SR-STF-0 and the SR-STF-40 at 7×10^3 s^{-1} are 9.03 MPa and 12.95 MPa, which are 4.69 and 25.82 times of these at 10^{-1} s^{-1}. It is interesting to note that there is a critical strain rate of 4.4×10^3 s^{-1} for all the composites, below which the stress increases with decreasing the mass fraction of STF microcapsules. However, the stresses of the composites increase with increasing the mass fraction of STF microcapsules, validating the experimental hypothesis as given by Fig. 8. Therefore, the composites with STF microcapsules realize sufficient flexibility under low strain rates, but a high impact resistance under high strain rates, making it a useful candidate for flexible protective structures.

It should be noted that the increase of the mass fraction of STF microcapsules will increase the density of the SR-STF composites. The densities of the SR-STF-0, the SR-STF-10, the SR-STF-20, the SR-STF-30, and the SR-STF-40 are 1.04, 1.07, 1.11, 1.15, and 1.20 g/cm^3, respectively. In practical application, for example the bulletproof helmet lining, the total weight is generally small, and therefore the slightly increase in weight is usually acceptable while using the SR-STF-40 instead of the SR-STF-0. In addition, the competition between the strength requirements and the lightweight requirements of materials can be expressed as

$$\kappa = \frac{(\sigma_{C\%} - \sigma_{0\%})/\sigma_{0\%}}{(\rho_{C\%} - \rho_{0\%})/\rho_{0\%}} \tag{26}$$

where $\sigma_{C\%}$ and $\rho_{C\%}$ are stress at strain 0.35 and density for the SR-STF composites with C% mass fraction of STF microcapsules, respectively; $\sigma_{0\%}$ and $\rho_{0\%}$ are stress at strain 0.35 and density for the pure SR material, respectively. For $\kappa > 1$, the increase of stiffness is faster than that of weight. Based on the prediction of the constitutive model, the stresses of the SR-STF-0, the SR-STF-10, the SR-STF-20, the SR-STF-30, and the SR-STF-40 at strain 0.35 under 7000 s^{-1} are 9.03, 10.01, 10.99, 11.97, and 12.95 MPa, respectively. According to Eq. (26), κ are 3.76, 3.22, 3.08, and 2.82 for the SR-STF-10, the SR-STF-20, the SR-STF-30, and the SR-STF-40, respectively, indicating that the increase of stiffness of the SR-STF composites is much faster than that of weight when compared to the pure SR, which is favorable for protective materials subjected to high velocity impact.

The composites with different contents of STF microcapsules have the same critical strain rate of 4.4×10^3 s^{-1}, implying that the critical strain rate may be determined by the properties of the STF. The diameter of the microcapsules could also influence the critical strain rate of the composites, which will be investigated in future. It is to be noted that beside the mass fraction of the microcapsules, the mechanical behavior of the SR-STF composites including the strain hardening, the strain rate sensitivity, and the critical strain rate should be affected by the shear-thickening behavior of the STF. In addition, it might also be dependent to the size and the distribution of the STF microcapsules. These effects will be investigated by experiments and numerical simulation in future.

5. Conclusions

In this paper, the silicone rubber composites with different contents of STF microcapsules are fabricated for the first time, and the mechanical behavior under various loading conditions is investigated. The main conclusions are as follows.

1. The spherical STF microcapsules with diameters ranging from 5 to 25 μm are successfully dispersed evenly and sealed firmly in the silicone rubber matrix through emulsifying and curing processes, providing a practical strategy for engineering applications of STF.
2. The SR-STF composites show obvious strain hardening and strain-rate strengthening effects due to the shear thickening and possible compressive jamming of the STF inside the microcapsules under high loading rates.
3. The stiffness of the SR-STF composites increases with decreasing the content of STF microcapsules under low strain rate. However, the stiffness of the composite with high STF microcapsules trends to exceed the other composites under high loading rates.
4. A hyper-viscoelastic constitutive model considering the effects of strain hardening, strain-rate strengthening, and content of STF microcapsules is developed, which is validated by experimental results.
5. A critical strain rate of about 4.4×10^3 s^{-1} is predicted by the constitutive model, above which the influence of the content of STF microcapsules on the stiffness of the SR-STF composite reverses, showing intelligent adaptation of the composites subjected to various impact loadings.

Author statements

J.Q. Zhu: Investigation, Writing - Original Draft. Z.P. Gu: Investigation, Formal analysis, Writing - Original Draft. Z.P. Liu: Methodology, Validation, Funding acquisition. F.C. Zhong: Writing - Review & Editing. X.Q. Wu: Conceptualization, Methodology, Writing - Review & Editing, Supervision, Funding acquisition. C.G. Huang: Writing - Review & Editing, Funding acquisition.

Declaration of competing interest

The authors declare that they have no known competing financial interests or personal relationships that could have appeared to influence the work reported in this paper.

Data availability

Data will be made available on request.

Acknowledgments

This work was supported by the National Natural Science Foundation of China (Grant Nos. 12272391, 12232020, and 51803197).

References

[1] Talreja K, Chauhan I, Ghosh A, Majumdar A, Butola BS. Functionalization of silica particles to tune the impact resistance of shear thickening fluid treated aramid fabrics. RSC Adv 2017;7(78):49787–94.
[2] Fang W, Yang X, Xu X, Li W, Li Q. Quasi-static and low-velocity impact responses of polypropylene random copolymer composites with adjustable crystalline structures. Compos B Eng 2021;224:109139.
[3] Tian Y, Yang R, Gu Z, Zhao H, Wu X, Dehaghani ST, et al. Ultrahigh cavitation erosion resistant metal-matrix composites with biomimetic hierarchical structure. Compos B Eng 2022;234:109730.
[4] Shi S, Si Y, Han Y, Wu T, Iqbal MI, Fei B, et al. Recent progress in protective membranes fabricated via electrospinning: advanced materials, biomimetic structures, and functional applications. Adv Mater 2022;34(17):2107938.
[5] Gopinath G, Zheng JQ, Batra RC. Effect of matrix on ballistic performance of soft body armor. Compos Struct 2012;94(9):2690–6.
[6] Alabbad M, Vel SS, Lopez-Anido RA. Computational model for predicting the low-velocity impact resistance and tolerance of composite laminates. Compos B Eng 2022;244:110187.
[7] Laha A, Majumdar A. Interactive effects of p-aramid fabric structure and shear thickening fluid on impact resistance performance of soft armor materials. Mater Des 2016;89:286–93.
[8] Cao SS, Pang HM, Zhao CY, Xuan SH, Gong XL. The CNT/PSt-EA/Kevlar composite with excellent ballistic performance. Compos B Eng 2020;185:107793.

[9] Bajya M, Majumdar A, Butola BS, Verma SK, Bhattacharjee D. Design strategy for optimising weight and ballistic performance of soft body armour reinforced with shear thickening fluid. Compos B Eng 2020;183:107721.
[10] Hu QF, Lu GX, Hameed N, Tse KM. Dynamic compressive behaviour of shear thickening fluid-filled honeycomb. Int J Mech Sci 2022;229:107493.
[11] Khodadadi A, Liaghat G, Taherzadeh-Fard A, Shahgholian-Ghahfarokhi D. Impact characteristics of soft composites using shear thickening fluid and natural rubber-A review of current status. Compos Struct 2021;271:114092.
[12] Gürgen S, Sofuoglu MA. Vibration attenuation of sandwich structures filled with shear thickening fluids. Compos B Eng 2020;186:107831.
[13] Zhao CY, Gong XL, Wang S, Jiang WQ, Xuan SH. Shear stiffening gels for intelligent anti-impact applications. Cell Rep Phys Sci 2020;1(12):100266.
[14] Zhang S, Wang S, Hu T, Xuan S, Jiang H, Gong X. Study the safeguarding performance of shear thickening gel by the mechanoluminescence method. Compos B Eng 2020;180:107564.
[15] Wei MH, Lin K, Sun L. Shear thickening fluids and their applications. Mater Des 2022;216:110570.
[16] Fan T, Sun Z, Zhang Y, Li Y, Chen Z, Huang P, et al. Novel Kevlar fabric composite for multifunctional soft body armor. Compos B Eng 2022;242:110106.
[17] Zhang X, Wang PF, Kurkin A, Chen Q, Gong XL, Zhang Z, et al. Mechanical response of shear thickening fluid filled composite subjected to different strain rates. Int J Mech Sci 2021;196:106304.
[18] Yu KJ, Cao HJ, Qian K, Sha XF, Chen YP. Shear-thickening behavior of modified silica nanoparticles in polyethylene glycol. J Nanoparticle Res 2012;14(3). 747.
[19] Lin G, Li J, Li F, Chen P, Sun W. Low-velocity impact response of sandwich composite panels with shear thickening gel filled honeycomb cores. Compos Commun 2022;32:101136.
[20] Khodadadi A, Liaghat G, Vahid S, Sabet AR, Hadavinia H. Ballistic performance of Kevlar fabric impregnated with nanosilica/PEG shear thickening fluid. Compos B Eng 2019;162:643–52.
[21] Fan T, Xue S-S, Zhu W-B, Zhang Y-Y, Li Y-Q, Chen Z-K, et al. Multifunctional polyurethane composite foam with outstanding anti-impact capacity for soft body armors. Acs Appl Mater Inter 2022;14(11):13778–89.
[22] Hoffman RL. Explanations for the cause of shear thickening in concentrated colloidal suspensions. J Rheol 1998;42(1):111–23.
[23] Cheng X, McCoy JH, Israelachvili JN, Cohen I. Imaging the microscopic structure of shear thinning and thickening colloidal suspensions. Science 2011;333(6047):1276–9.
[24] Brown E, Jaeger HM. Through thick and thin. Science 2011;333(6047):1230–1.
[25] Zhang JS, Wang Y, Deng HX, Zhou JY, Liu S, Wu JP, et al. A high anti-impact STF/Ecoflex composite structure with a sensing capacity for wearable design. Compos B Eng 2022;233:109656.
[26] Waitukaitis SR, Jaeger HM. Impact-activated solidification of dense suspensions via dynamic jamming fronts. Nature 2012;487(7406):205–9.
[27] Wu XQ, Zhong FC, Yin QY, Huang CG. Dynamic response of shear thickening fluid under laser induced shock. Appl Phys Lett 2015;106(7):071903.
[28] Jiang WF, Gong XL, Xuan SH, Jiang WQ, Ye F, Li XF, et al. Stress pulse attenuation in shear thickening fluid. Appl Phys Lett 2013;102(10):101901.
[29] Hsu CP, Mandal J, Ramakrishna SN, Spencer ND, Isa L. Exploring the roles of roughness, friction and adhesion in discontinuous shear thickening by means of thermo-responsive particles. Nat Commun 2021;12(1):1477.
[30] Wu XQ, Yin QY, Huang CG. Experimental study on pressure, stress state, and temperature-dependent dynamic behavior of shear thickening fluid subjected to laser induced shock. J Appl Phys 2015;118(17):173102.
[31] Qin JB, Guo BR, Zhang L, Wang TW, Zhang GC, Shi XT. Soft armor materials constructed with Kevlar fabric and a novel shear thickening fluid. Compos B Eng 2020;183:107686.
[32] Qin JB, Zhang GC, Shi XT, Tao M. Study of a shear thickening fluid: the dispersions of silica nanoparticles in 1-butyl-3-methylimidazolium tetrafluoroborate. J Nanoparticle Res 2015;17(8).
[33] Peng GR, Li WH, Tian TF, Ding J, Nakano M. Experimental and modeling study of viscoelastic behaviors of magneto-rheological shear thickening fluids. Korea Aust Rheol J 2014;26(2):149–58.
[34] Balali E, Kordani N, Vanini AS. Response of glass fiber-reinforced hybrid shear thickening fluid (STF) under low-velocity impact. J Textil Inst 2017;108(3):376–84.
[35] Lin K, Zhou AN, Liu HJ, Liu Y, Huang CC. Shear thickening fluid damper and its application to vibration mitigation of stay cable. Structures 2020;26:214–23.
[36] Mawkhlieng U, Majumdar A. Deconstructing the role of shear thickening fluid in enhancing the impact resistance of high-performance fabrics. Compos B Eng 2019;175:107167.
[37] Arora S, Majumdar A, Butola BS. Structure induced effectiveness of shear thickening fluid for modulating impact resistance of UHMWPE fabrics. Compos Struct 2019;210:41–8.
[38] Gürgen S, Fernandes FAO, de Sousa Rja, Kushan MC. Development of eco-friendly shock-absorbing cork composites enhanced by a Non-Newtonian fluid. Appl Compos Mater 2021;28(1):165–79.
[39] Gürgen S, Kushan MC, Li WH. Shear thickening fluids in protective applications: a review. Prog Polym Sci 2017;75:48–72.
[40] Gürgen S, Sofuoglu MA. Experimental investigation on vibration characteristics of shear thickening fluid filled CFRP tubes. Compos Struct 2019;226:111236.
[41] Gu ZP, Wu XQ, Li QM, Yin QY, Huang CG. Dynamic compressive behaviour of sandwich panels with lattice truss core filled by shear thickening fluid. Int J Impact Eng 2020;143:103616.
[42] Wu XQ, Xiao KL, Yin QY, Zhong FC, Huang CG. Experimental study on dynamic compressive behaviour of sandwich panel with shear thickening fluid filled pyramidal lattice truss core. Int J Mech Sci 2018;138:467–75.
[43] Stober W, Fink A, Bohn E. Controlled growth of monodisperse silica spheres in micron size range. J Colloid Interface Sci 1968;26(1):62–9.
[44] Stark WJ, Stoessel PR, Wohlleben W, Hafner A. Industrial applications of nanoparticles. Chem Soc Rev 2015;44(16):5793–805.
[45] Omidvar M, Iskander M, Bless S. Stress-strain behavior of sand at high strain rates. Int J Impact Eng 2012;49:192–213.
[46] Tang Y, Zhang W, Jiang X, Zhao J, Xie W, Chen T. Experimental investigations on phenomenological constitutive model of closed-cell PVC foam considering the effects of density, strain rate and anisotropy. Compos B Eng 2022;238:109885.
[47] Chen W, Lu F, Frew DJ, Forrestal MJ. Dynamic compression testing of soft materials. J Appl Mech-T Asme 2002;69(3):214–23.
[48] Forrestal MJ, Wright TW, Chen W. The effect of radial inertia on brittle samples during the split Hopkinson pressure bar test. Int J Impact Eng 2007;34(3):405–11.
[49] Song B, Ge Y, Chen WW, Weerasooriya T. Radial inertia effects in Kolsky bar testing of extra-soft specimens. Exp Mech 2007;47(5):659–70.
[50] Liu F, Li Q. Strain-rate effect of polymers and correction methodology in a SHPB test. Int J Impact Eng 2022;161:104109.
[51] Irfan MA, Prakash V. Time resolved friction during dry sliding of metal on metal. Int J Solid Struct 2000;37(20):2859–82.
[52] Kariem MA, Santiago RC, Govender R, Shu DW, Ruan D, Nurick G, et al. Round-Robin test of split Hopkinson pressure bar. Int J Impact Eng 2019;126:62–75.
[53] Malinowski JZ, Klepaczko JR, Kowalewski ZL. Miniaturized compression test at very high strain rates by direct impact. Exp Mech 2007;47(4):451–63.
[54] Malinowski JZ, Klepaczko JR. A unified analytic and numerical approach to specimen behavior in the split-hopkinson pressure bar. Int J Mech Sci 1986;28(6):381–91.
[55] Zhao CY, Xu CH, Cao SS, Xuan SH, Jiang WQ, Gong XL. Anti-impact behavior of a novel soft body armor based on shear thickening gel (STG) impregnated Kevlar fabrics. Smart Mater Struct 2019;28(7):075036.
[56] Yang LM, Shim VPW, Lim CT. A visco-hyperelastic approach to modelling the constitutive behaviour of rubber. Int J Impact Eng 2000;24(6–7):545–60.
[57] Li CY, Lua J. A hyper-viscoelastic constitutive model for polyurea. Mater Lett 2009;63(11):877–80.
[58] Pouriayevali H, Guo YB, Shim VPW. A constitutive description of elastomer behaviour at high strain rates - a strain-dependent relaxation time approach. Int J Impact Eng 2012;47:71–8.
[59] Ogden RW. Large deformation isotropic elasticity - correlation of theory and experiment for compressible rubberlike solids. Proc Roy Soc Lond 1972;328(1575):567–83.
[60] Gu ZP, Cheng YJ, Xiao KL, Li K, Wu XQ, Li QM, et al. Geometrical scaling law for laser-induced micro-projectile impact testing. Int J Mech Sci 2022;223:107289.